Analysis of Band-Pass Filter Characteristics in a Ferrite Device with Carbon Nanotube Electrodes

Toshihito Umegaki, Matsuto Ogawa, and Tanroku Miyoshi
Department of Electrical and Electronics Engineering
Kobe University
Kobe City, 657-8501, Japan

ABSTRACT

We have studied magnetostatic waves excited and received by carbon nanotubes in the high-frequency band-pass filter on yttrium iron garnet (YIG). First, we have analyzed dispersion curves of magnetostatic waves in YIG based upon the magnetostatic approximation method. We have studied the characteristics of the band-pass filter where the high-frequency current flowing on single-wall CNTs may excite and receive directly magnetostatic waves in the ferrite film beneath them. Next, we have studied the device where the current is flowing on bundle CNTs. It is found that band-pass filter characteristics, such as the insertion loss (*IL*), the center frequency (f_0), and bandwidth (*BW*) are significantly controlled by both the chirality of the CNTs and the numbers of CNTs in the bundle CNTs. On these results, we have proposed a novel ferrite device which may work to discriminate the chirality of CNTs and the numbers of CNTs in a bundle CNT. In this device, the chirality or the number of CNTs in a bundle CNT may be measured by means of the band-pass characteristics via the wavelength of the operating magnetostatic waves.

I. INTRODUCTION

Many types of magnetostatic wave devices have been reported as small microwave devices such as delay lines, filters, and oscillators, where operating wavelength is ranging from 10^{-5} m to 10^{-8} m [1, 2]. Their operating frequency depends on the dimension of electrodes to excite magnetostatic waves and it is restricted within fabrication accuracy. On the other hand, since the discovery of carbon nanotubes (CNTs) [3], the properties of CNTs have attracted much interest due to their unique structures and promising electrical properties. Especially the diameters of CNTs can be easily controlled as small as several nanometers. In addition, the great advantage of CNTs over conventional materials is that they have ballistic conductivities and diameter control can be achieved by means of self-organization. As an application to make use of the characteristics, we investigate the High-Frequency (HF) filters using CNTs for electrodes to excite magnetostatic waves in ferrite devices. Compared with the case of the HF filters with conventional metal-electrodes [1, 2], the CNT electrodes may improve the operating frequency up to THz region. As the operating frequency of such devices increases, we can realize devices which can handle more information than conventional ones.

In this paper, we study magnetostatic waves excited and received by CNTs in yttrium iron garnet (YIG). We analyze dispersion curves of magnetostatic waves in YIG based upon the magnetostatic approximation method. It is found that, at the frequency in THz domain, magnetostatic waves propagate with wavelength as short as several nanometers. We study the band-pass filter characteristics of the YIG device where the high-frequency current flowing on single-wall CNTs, which are treated as cylindrical electrodes but reflecting the results of quantum transport analysis. The CNT electrodes may excite and receive directly magnetostatic waves in the ferrite film beneath them.

In the following sections, we study the high frequency characteristics of the device based upon the magnetostatic approximation. The dispersion curves show the operating frequency is ranging from GHz region to THz, and the wavelength is ranging longer than a few nm. Then we analyze the filter characteristics of the device with single wall CNTs or with bundle CNTs. In order to excite and receive magnetostatic waves efficiently by high frequency current in CNTs, we may have to construct practical structures of CNTs to overcome

attenuation of magnetostatic waves and to avoid other electromagnetic couplings between CNTs.

In this paper, however, we treat the CNT as realistic quantum wire. It is found that band-pass filter characteristics, such as the insertion loss (*IL*), the band-pass center frequency (f_0), and bandwidth (*BW*) are significantly controlled by both the chirality of the CNTs and the numbers of CNTs in a bundle CNT, which are used as electrodes. On these results, we propose a novel ferrite device, which will discriminate the chirality of CNTs and the numbers of CNTs in a bundle CNT. In this device, the chirality or the number of CNTs in a bundle CNT may be measured by means of the band-pass characteristics via the wavelength of the operating magnetostatic waves. In the final section, conclusions are summarized.

II. A FERRITE DEVICE WITH SINGLE-WALL CARBON NANOTUBES

A. Theoretical Analysis

Consider a ferrite based HF filter using CNTs for electrodes to excite magnetostatic waves, whose schematic structure is shown in Fig. 1. The high-frequency current flowing through one single-wall CNT excites directly magnetostatic waves in a ferrite film and the other single-wall CNT receives them. Although the distance between the two electrodes *v* is not a parameter in our calculation, we may have to control *v* in practical structures of CNTs to overcome attenuation of magnetostatic waves and to avoid other electromagnetic couplings between CNTs. Fig. 2 shows a cross-sectional view of the device model with a single-wall CNT, where *r* is radius of the CNT, and *t* is the thickness of YIG. We can grow CNTs in various processes. One of the processes provides good selectivity to control the single-walled CNT average diameter within angstrom accuracy. In the future, we will be able to grow CNTs not only with the selectivity but also in good accuracy of the growing position [4,5] to fabricate this kind of devices.

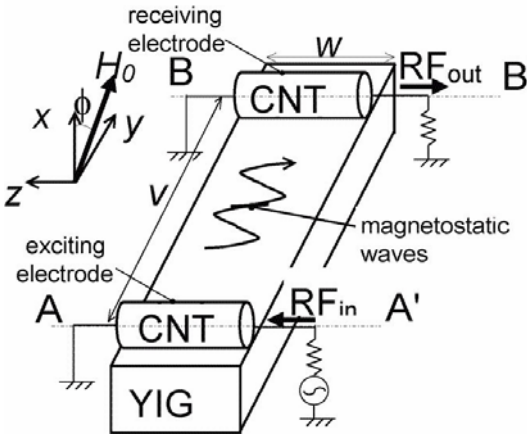

Fig.1. The schematic structure of the device: Straight lines A-A' and B-B' coincide with the axes of CNTs supplied with RF_{in} and detected RF_{out} current, respectively. The line A-A' is parallel to the line B-B' and distance between them is *v*.

When a bias magnetic field H_0 is applied obliquely from *x*-axis of the angle ϕ (Fig. 1), magnetic permeability is expressed in the following tensor form (see Appendix B):

$$\hat{\mu} = \begin{pmatrix} \bar{c}^2 + \mu\bar{s}^2 & (1-\mu)\,\bar{s}\bar{c} & -j\kappa\bar{s} \\ (1-\mu)\,\bar{s}\bar{c} & \bar{s}^2 + \mu\bar{c}^2 & j\kappa\bar{s} \\ j\kappa\bar{s} & -j\kappa\bar{c} & \mu \end{pmatrix}, \tag{1}$$

where

$$\bar{c} \equiv \cos\phi, \quad \bar{s} \equiv \sin\phi, \tag{2}$$

$$\mu = \frac{[\omega_h + \omega_{he}(\beta)][\omega_h + \omega_j + \omega_{he}(\beta)] - \omega^2}{[\omega_h + \omega_{he}(\beta)]^2 - \omega^2}, \tag{3}$$

$$\kappa = \frac{\omega\omega_j}{[\omega_h + \omega_{he}(\beta)]^2 - \omega^2}, \tag{4}$$

$$\omega_{he}(\beta) = 2\omega_e(1 - \cos\beta a), \tag{5}$$

$$\omega_j = \gamma\mu_0 M_0, \quad \omega_h = \gamma\mu_0 H_0, \quad \omega_e = \gamma\mu_0 H_e. \tag{6}$$

β is the propagation constant of magnetostatic waves, ω is angular frequency, γ is called the gyromagnetic ratio which is 1.759×10^{11} m^2/Wbs, H_0 is the bias magnetic field, M_0 is the saturation magnetization, *a* is the lattice constant of YIG which is 1.238nm, and H_e corresponds to Weiss's molecular field [6], respectively.

In the present simulation, current flow and displacement current are negligibly small compared to $|\nabla \times H|$, where **H** is the magnetic field. Therefore we can adopt the magnetostatic approximation [2, 7, 8]. In the magnetostatic approximation, **H** is represented as the gradient of a magnetostatic potential ψ, namely

$$\mathrm{H} = -\nabla\psi$$

The magnetic flux density **B** is $\mu_0\hat{\mu}\mathrm{H}$. From

$$\nabla \bullet \mathrm{B} = 0$$

we can obtain an equation for ψ:

$$(\bar{c}^2+\mu\bar{s}^2)\frac{\partial^2\psi}{\partial x^2}+2(1-\mu)\bar{c}\bar{s}\frac{\partial^2\psi}{\partial x\partial y}+(\bar{s}^2+\mu\bar{c}^2)\frac{\partial^2\psi}{\partial y^2}=0. \quad (7)$$

To solve this equation for our device configuration, we have sliced the region under consideration into 2*N* pieces parallel to the *y*-axis as shown in Fig. 2. Then we can obtain ψ as follows:

$$\psi_{2N}=\int_{-\infty}^{\infty}A_{2N}e^{-|\beta|(x-r)}e^{-j\beta y}d\beta, \quad (8a)$$

$$\psi_i=\int_{-\infty}^{\infty}(A_ie^{-|\beta|\bar{x}_i}+B_ie^{|\beta|\bar{x}_i})e^{-j\beta y}d\beta, \quad (8b)$$

$$\bar{x}_i=x-x_i,\quad (i=0,1,2,\cdots,2N-1)\ , \quad (8c)$$

$$x_i=r\cos\frac{\pi i}{2N}, \quad (8d)$$

$$\psi_{\mathrm{f}}=\int_{-\infty}^{\infty}(Ce^{jk_1^x\bar{x}}+De^{jk_2^x\bar{x}})e^{-j\beta y}d\beta, \quad (8e)$$

$$\bar{x}=x+r, \quad (8f)$$

$$k_l^x=|\beta|\frac{(1-\mu)\bar{s}\bar{c}s\mp\sqrt{-\mu}}{\bar{c}^2+\mu\bar{s}^2},\quad (l=1,2), \quad (8g)$$

$$s=\frac{\beta}{|\beta|}, \quad (8h)$$

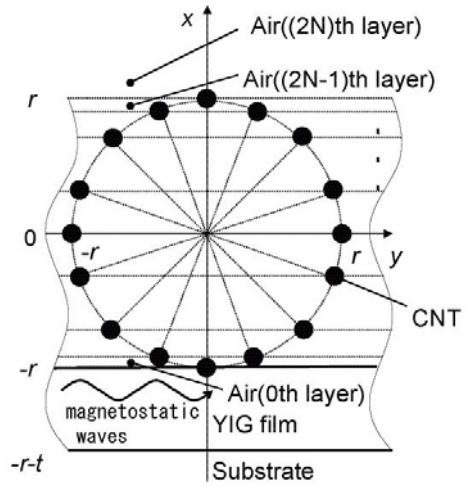

Fig. 2. A cross-sectional view of the schematic device model with a single-wall CNT centering around the line A-A' or B-B': The magnetostatic wave is excited by the CNT (A-A') and received by B-B' as shown in Fig. 1. In the cross section, we apply the Boundary Conditions at the infinite current points, normal (*x*) component of magnetic flux density is continuous and tangential (*y*) components of magnetic field and current are continuous. The closed circles are current points arranged at equal interval on a circle centered at the origin of *x* and *y* coordinates.

$$\psi_{\mathrm{sub}}=\int_{-\infty}^{\infty}Ee^{|\beta|(x+r+t)}e^{-j\beta y}d\beta, \quad (8i)$$

where the index of each ψ represents to be each region along the *x*-axis and *t* is the thickness of the YIG film as shown in Fig. 2. The subscript f stands for the YIG film and sub is the substrate. A_i and B_i (*i*=0, 1,…,2*N*) are amplitudes in *i* th air layer decaying toward + and - *x* directions, respectively. *C* and *D* are amplitudes in the YIG film propagating toward + and - *x* directions, respectively. *E* is amplitude in the substrate decaying toward -*x* direction.

Applying the continuity conditions of the normal (*x*) components of the magnetic flux density (B_i^x, *i*=0, 1, ...,2*N*, B_f^x, B_{sub}^x), tangential *y* components of the magnetic field (H_i^y, *i*=0, 1, ... ,2*N*, H_f^y, H_{sub}^y) and current density J_i^z, *i*=0, 1, ... ,2*N* as

$$\begin{aligned}
&H_{2N}^y-H_{2N-1}^y=J_{2N}^z\big|_{x=r},\\
&B_{2N}^x-B_{2N-1}^x=0\big|_{x=r},\\
&H_i^y-H_{i-1}^y=J_i^z\big|_{x=x_i},\\
&B_i^x-B_{i-1}^x=0\big|_{x=x_i},\quad (i=0,1,\cdots,2N-1)\\
&H_0^y-H_{\mathrm{f}}^y=J_0^z\big|_{x=-r},\\
&B_0^x-B_{\mathrm{f}}^x=0\big|_{x=-r},\\
&H_{\mathrm{f}}^y-H_{\mathrm{sub}}^y=0\big|_{x=-r-t},\\
&B_{\mathrm{f}}^x-B_{\mathrm{sub}}^x=0\big|_{x=-r-t}.
\end{aligned} \quad (9)$$

The continuity conditions (9) are valid for the magnetostatic waves [2]. Substituting Eqs.(8) into Eqs.(9), we obtain the amplitude *D* in Eq.(8e) as

$$D=-\frac{\sum_{k=0}^{2N}e^{|\beta|(-r+x_k)}\tilde{J}_k^z(\beta)}{4\pi j\beta F(\omega,\beta)p(\omega,\beta)}, \quad (10)$$

where

$$\tilde{J}_k^z(\beta)\equiv\int_{-\infty}^{\infty}J_k^ze^{j\beta y}dy, \quad (11)$$

F and *p* will be shown in Eq. (13). All other amplitudes can be expressed in terms of *D*. For example, the amplitude *C* can be expressed as

$$C=\frac{jk_2^x-|\beta|}{-jk_1^x+|\beta|}e^{j(k_1^x-k_2^x)t}D. \quad (12)$$

When we take $F(\omega, \beta)$ as a zero, it should be calculated for the next two cases.

i) $k_3^x > 0$ or, for example, $\phi = 0$ (see Fig. 1),

$$F(\omega,\beta) = \tan\frac{k_3^x t}{2} - \frac{1}{\sqrt{-\mu}}, \qquad (13a)$$
$$p(\omega,\beta) = \frac{2\cos^2\frac{k_3^x t}{2}}{(\frac{\lambda}{\sqrt{-\mu}}-1)} e^{-j k_3^x t}(\tan\frac{k_3^x t}{2} + \sqrt{-\mu}).$$

ii) $k_3^x < 0$,

$$F(\omega,\beta) = \tan\frac{k_3^x t}{2} + \sqrt{-\mu}, \qquad (13b)$$
$$p(\omega,\beta) = \frac{2\cos^2\frac{k_3^x t}{2}}{(\frac{\lambda}{\sqrt{-\mu}}-1)} e^{-j k_3^x t}(\tan\frac{k_3^x t}{2} - \frac{1}{\sqrt{-\mu}}),$$

where $k_3^x = \frac{1}{2}\left(k_2^x - k_1^x\right)$. Although ϕ can be set any value, we set ϕ is zero throughout the paper for simplicity. CNTs with chiralities (n, 0) and (n, n) are called *zig-zag* and *armchair* types, respectively [9]. Since the current density is generally constant around the circumference of the single-wall CNT [10], it can be written as

$$J_i^z = \begin{cases} \frac{I_0}{4N}\delta(y), & i = 0 \\ \frac{I_0}{4N}\sum_{\pm}\delta(y \pm y_i), & i = 1,\cdots,2N-1 \\ \frac{I_0}{4N}\delta(y), & i = 2N \end{cases} \qquad (14a)$$

$$y_i = r\sin\left(\frac{\pi i}{2N}\right), \quad i = 0,1,2,\cdots,2N-1, \qquad (14b)$$

where I_0 is the amplitude of the total current flowing through the CNT, $\delta(y)$is the Dirac delta function. Then the amplitude D is expressed as follows using Bessel's integration formalism (see Appendix):

$$D = -\frac{I_0 e^{-|\beta|x}}{4\pi j\beta F(\omega,\beta)p(\omega,\beta)}. \qquad (15)$$

From Eqs. (8) and (15), the magnetostatic potential ψ can be determined as a residue with the pole of $F(\omega, \beta)$.

The electromagnetic power flowing different regions has been obtained using Poynting's theorem as

$$P^y = \frac{1}{2}\mathbf{Re}\left[\int_{-\infty}^{\infty}(-j\omega\psi^* B^y)dx\right], \qquad (16)$$

where ψ^* is the complex conjugate of ψ. From this power, the radiation resistance $R^{\pm}$ is defined as

$$R^{\pm}(\omega) = \left.\frac{2P^y w}{I_0^2}\right|_{s=\pm 1}, \qquad (17)$$

where w is the length of the CNT electrodes. The insertion loss IL is basically defined as the ratio of the input power and the output one of the device. It is a figure of merit of the device which is expressed as

$$IL = 10\log\frac{[R_g + R^+(\omega) + R^-(\omega) + R_c]^2}{4R_g R^+(\omega)}. \qquad (18)$$

In Eq. (18), R_g is the source resistance (50Ω). From the analysis of quantum transport in CNT [10], R_c is obtained as $1/2G_0$, where G_0 is the quantum conductance $2e^2/h$. $R^{\pm}(\omega)$ in Eq. (18) includes only the 1st order standing wave along the thickness of the YIG film, respectively. Note that the quantum conductance is included in Eq. (18), since we have used CNT as excitation electrodes. The propagation loss, and the reactance of the CNTs are neglected for simplicity. We evaluate insertion loss as one of the characteristic values of the device.

B. Numerical results

Figure 3 shows the simulated dispersion curves of magnetostatic waves propagating in y-direction of the device. In Fig. 3, the angle ϕ is set to 0, the thickness of YIG is 10nm, $\mu_0 M_0$ is 0.17T, and $\mu_0 H_0$ is 0.1T, respectively. The upper limit of the dispersion curves can be determined by the condition where the phase shift among each magnetization must be less than π. Then the operating frequency is limited less than 5THz. As the wavelength becomes 2.5nm, the operating frequency is 10^3 times as high as that in the present magnetostatic wave devices [1,2]. This high frequency operation can be achieved because Weiss's molecular field H_e strongly enhances the bias magnetic field. The solid line in Fig. 3 is a dispersion curve when $\mu_0 H_e$ is 46T [6]. The dotted dashed line and the broken line in Fig. 3 are the dispersion curves when $\mu_0 H_e$ is +/-10% larger than 46T, respectively.

Figure 4 shows the evidence in support of the validity of our calculation. We have applied our simulation model to a ferromagnetic material (nickel) and obtained the dispersion curves shown in Fig. 4. The solid line is obtained for the Weiss's molecular field of 317T [11], and the other two curves are for +/-10% larger field, respectively. The closed circles are reported experimental dispersion relation of the magnetostatic waves propagating in Ni [12]. Our results agree with the experimental results, although both the theoretical and experimental data are for Ni. Since our simulation

is based on the same theory ([11] and Appendix B) for spin magnetization that can be equally applied to ferromagnetic materials, the magnetostatic waves can be also excited in YIG in the frequency range obeying the dispersion curves predicted in Fig. 3. In order to excite magnetostatic waves effectively in the device configuration shown in Fig. 1, the width or diameter of the excitation electrode must be precisely designed and fabricated shorter than the wavelength of the magnetostatic waves [7]. In our case, since the wavelengths are ranging from several to a hundred nm, CNT electrodes are suitable for the excitation of the magnetostatic waves in the similar way as realized in the conventional devices [2,7].

Figure 5 is the simulated frequency dependence of the insertion loss (*IL*). In this figure, we have assumed *zig-zag* type CNTs for the electrodes with the metallic chirality (*n*,0), where *n*=30, 45, 90, and 120, respectively, and *w* is 1μm. As seen, this device works as a high-frequency band-pass filter

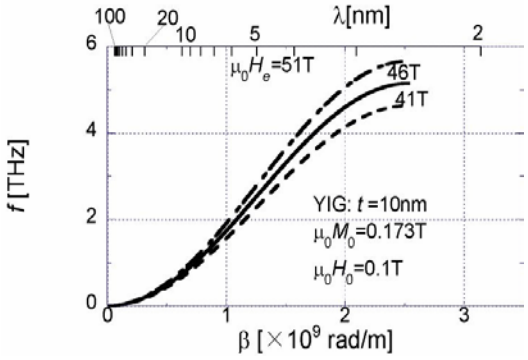

Fig. 3. Dispersion curves of the magnetostatic waves in THz domain excited in the YIG: Three dispersion curves are plotted. The solid line is obtained for Weiss's molecular field $\mu_0 H_e$ of 46T, and the other two curves are for +/-10 % larger field, respectively.

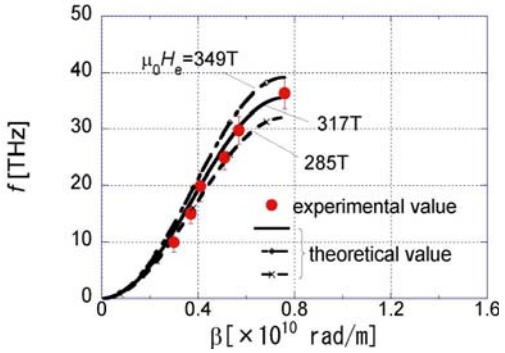

Fig. 4. Comparison of experimental dispersion curves with those obtained from the present simulation in Ni.

(BPF) in THz domain. Three characteristic values can be defined to specify the characteristics of this device: the minimum insertion loss IL_{min}, the center frequency f_0, and the bandwidth *BW* where *IL* is less than IL_{min} +3dB. When *n* is 30, we obtain IL_{min}=24.1dB, f_0=5.14THz, and *BW*=0.02THz (solid line), respectively. On the other hand, when *n* is 120, these values become IL_{min} =24.1dB, f_0=0.61THz, and *BW* =0.19THz (broken line), respectively.

Figure 6 shows the dependence of f_0 and *BW* on the chirality *n* of the CNTs. From this figure, it is found that when *n*, in other words, the diameter of the CNT increases, operating wavelength becomes longer and f_0 decreases. Taking the relationship between *n* and f_0 into account, we can design the characteristics of the BPF by means of the diameter of the CNT. However, since the *IL* is too large for practical application, we will analyze the characteristics of the BPF with bundle CNTs in the next section to improve the *IL* characteristics.

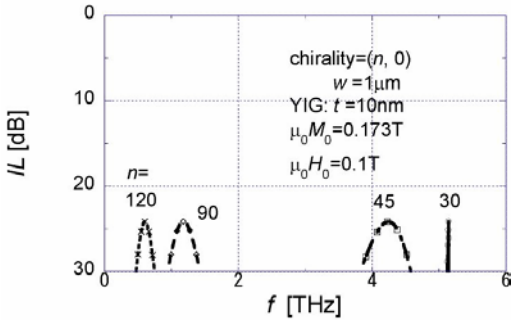

Fig. 5. The frequency dependence of the insertion loss *IL* for various *n*: When *n*=120, it is found that f_0=0.60THz and *BW*=0.19THz, respectively. When *n*=90, 45, and 30, we can find f_0 and *BW* in the same way.

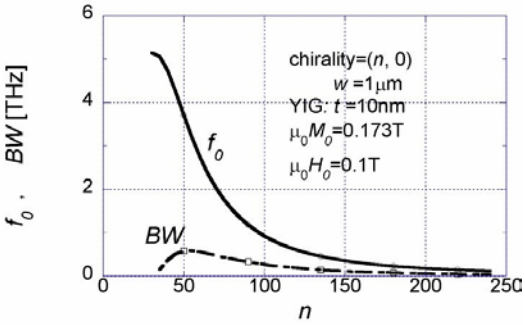

Fig. 6. The chirality (*n*)-dependence of the center frequency f_0 and bandwidth *BW* of the device: The f_0 monotonously decreases as *n* increases, whereas the *BW* becomes the maximum value as *n* is near 50.

III. A FERRITE DEVICE WITH BUNDLE CARBON NANOTUBES

A. Theoretical analysis of bundle carbon nanotubes

We consider the schematic structure of the device with the bundle CNTs instead of single-wall CNTs for electrodes of the HF filter as shown in Fig. 7 in order to improve the performance. Figure 8 shows a cross-sectional view of the device model with a bundle CNT, where r is the radius of each single-wall CNT, m is the numbers of CNTs along x and y-axes, respectively.

Same as the previous section, to solve Eq. (7) for the device configuration, we have sliced the region into $2mN$ pieces parallel to the y-axis as shown in Fig. 8. Then we can obtain ψ in each slice as follows:

$$\psi_{2mN} = \int_{-\infty}^{\infty} A_{2mN} e^{-|\beta|[x-(2m-1)r]} e^{-j\beta y} d\beta \quad (19a)$$

$$\psi_i = \int_{-\infty}^{\infty} (A_i e^{-|\beta|(x-x_i)} + B_i e^{|\beta|(x-x_i)}) e^{-j\beta y} d\beta \quad (19b)$$

$$i = 0, 1, 2, \cdots, 2mN-1, 2mN \quad (19c)$$

$$x_i = -r\cos\frac{\pi i}{2N}(-1)^{int(\frac{i-1}{2N})} + 2r \cdot int(\frac{i-1}{2N}), \quad (19d)$$

$$\psi_{\mathrm{f}} = \int_{-\infty}^{\infty} (Ce^{jk_1^x(x+r)} + De^{jk_2^x(x+r)}) e^{-j\beta y} d\beta \quad (19e)$$

$$k_l^x = |\beta| \frac{(1-\mu)\bar{s}\bar{c}s \mp \sqrt{-\mu}}{\bar{c}^2 + \mu\bar{s}^2}, \quad (l = 1, 2) \quad (19f)$$

$$s = \frac{\beta}{|\beta|}, \quad (19g)$$

$$\psi_{\mathrm{sub}} = \int_{-\infty}^{\infty} Ee^{|\beta|(x+r+t)} e^{-j\beta y} d\beta, \quad (19h)$$

where the index of each ψ represents each region along the x-axis in Fig. 8.

Applying the same continuity conditions as in Eq. (9), we determine the amplitude D in Eq. (19e) as

$$D = -\frac{\sum_{i=0}^{2mN} e^{|\beta|(x_0 - x_i)} \tilde{J}_i^z(\beta)}{4\pi j\beta F(\omega,\beta) p(\omega,\beta)}, \quad (20)$$

where J_i^z is given by the following equation instead of Eq. (14a).

$$J_i^z = \begin{cases} I_0 \sum_{j=1}^{m} \frac{\delta(y - y_{i,j,1})}{4m^2 N}, i = 0, 2mN \\ I_0 \sum_{j=1}^{m} \frac{\delta(y - y_{i,j,1})}{2m^2 N}, i = 2N, \cdots, 2(m-1)N \\ I_0 \sum_{j=1}^{m} \sum_{k=1}^{2} \frac{\delta(y - y_{i,j,k})}{4m^2 N}, i = \text{others} \end{cases} \quad (21)$$

where

$$y_{i,j,k} = r\left[2(j-1) - (-1)^k \sin\frac{\pi i}{2N}\right]. \quad (22)$$

The amplitude D is expressed as follows using Bessel's integration formalism same as the derivation of Eq. (15):

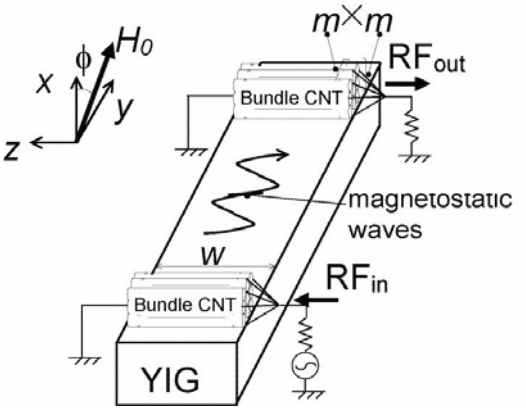

Fig. 7. The schematic structure of the device: The high-frequency current flowing through one bundle CNT excites directly magnetostatic waves in a ferrite film and the other bundle CNT receives them. Each bundle CNT consists of the m^2 parts of the single-wall CNTs arranged along x and y directions, respectively.

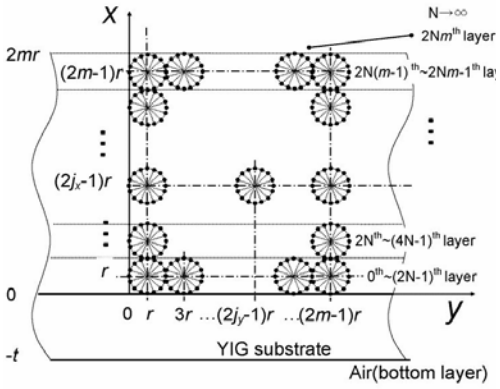

Fig. 8. A cross-sectional view of the schematic device model with a bundle multi-wall CNT: The m^2 CNTs, each of which is same as shown in Fig. 2, are aligned along x and y directions, respectively.

$$D = -\frac{I_0 \sum_{l'=1}^{m} e^{2j(l'-1)\beta r} \sum_{l=1}^{m} e^{-2(l-1)|\beta| r} e^{-|\beta| r}}{4\pi m^2 j\beta F(\omega,\beta) p(\omega,\beta)}. \quad (23)$$

All other amplitudes can be expressed in terms of D. From Eqs. (19), and (23), the magnetostatic potential ψ can be obtained as a residue with the pole of $F(\omega, \beta)$. The electromagnetic power flowing in different regions, the radiation resistance $R^{\pm}$, and the insertion loss IL are given by Eqs. (16), (17), and (18), respectively. In Eq. (18), R_c is given by $1/2m^2G_0$ for the bundle CNT. R_g and other conditions are same as the case of single-wall CNT electrodes as shown in previous section.

B. Numerical results

Figure 9 shows the frequency dependence of the IL. In Fig. 9, the product of the chirality n and the numbers of the CNTs m is kept to be constant, that is nm=300. We assume the bundle *zig-zag* type CNTs have the metallic chirality (300/m, 0) with the parameter m=1, 10, 20, 50, respectively. When m=1, we have found IL_{min}=27.5dB and f_0=4.4THz (solid line in Fig. 9). On the other hand, when m=50, it is found that IL_{min} =9.0dB and f_0 = 1.2THz (broken line in Fig. 9). Note that the insertion loss IL is significantly improved with the use of the bundle CNTs compared with the case of the single-wall CNT electrodes.

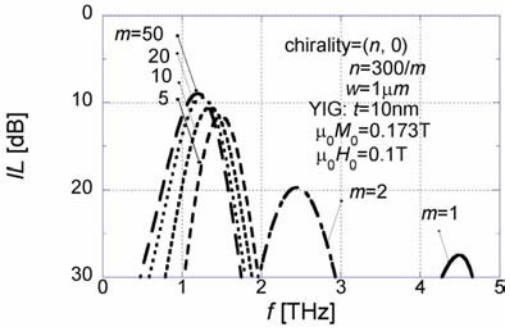

Fig. 9. The frequency dependence of the insertion loss IL for various m: When m=50, it is found that IL_{min}=9.0dB, f_0=1.2THz and BW=0.4THz, respectively. When m=20, 10, 5, 2, and 1, we can find IL_{min}, f_0, and BW in the same way.

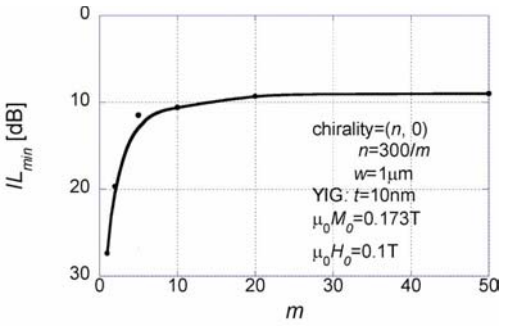

Fig. 10: The m-dependence of the minimum insertion loss IL_{min}: The IL_{min} monotonously increases as m increases.

Figure 10 shows the m-dependence of the IL_{min}. From this figure, it is found that when m and the dimension of the bundle CNT increase, IL_{min} becomes smaller. Because there is a relation between IL_{min} and impedance matching and the matching condition is improved by R_c in Eq. (18), we can improve both the IL and the impedance matching condition by using the bundle CNTs instead of single-wall CNTs. Figure 11 shows the m-dependence of f_0. When m or the dimension of the bundle CNT increases, operation wavelength becomes longer and f_0 decreases. But f_0 is almost independent of m when m becomes larger than 20.

Since we have kept the product nm to be constant (nm =300), the main reason of this m-dependence is that only CNTs on the surface of the YIG substrate efficiently excite the magnetostatic

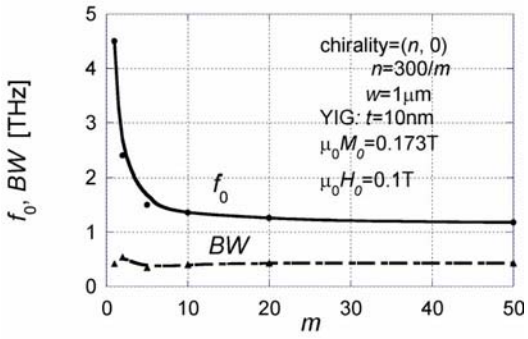

Fig. 11. The m-dependence of the f_0 and BW: The f_0 monotonously decreases as m increases, whereas the BW is almost independent of m.

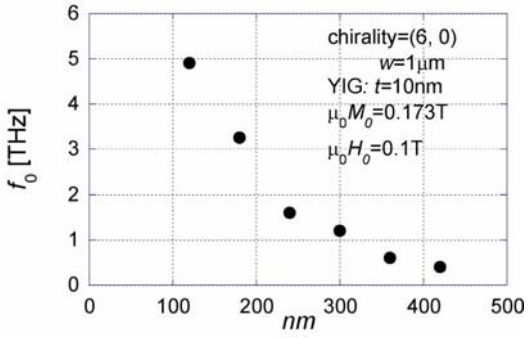

Fig. 12. The nm-dependence of the f_0: The f_0 monotonously decreases as the product nm increases.

waves, but on the other hand, CNTs far from the surface are less effective for the excitation. When the numbers m is less than 20, f_0 strongly depends on m since each CNT has a large diameter and the excitation mainly occurs at the point of contact between each CNT and the YIG surface. On the other hand, as the number m becomes larger, the diameter of each CNT becomes smaller and the distance between each contact point becomes smaller. When m exceeds 20, the excitation occurs almost everywhere on the YIG surface because the distance between each contact point is less than 1.2nm. Therefore, even when m becomes larger than 20, the characteristics do not change drastically.

On the contrary, the product nm significantly affects the performance of the device. Figure 12 shows the nm dependence of the f_0. The product nm has the obvious relations with the f_0 and we can design the characteristics of the BPF by means of dimension of the bundle CNT. Reversely, these characteristics enable us to discriminate nm by measuring the $IL_{\min}$, f_0, and BW of the BPF. The BPF with the bundle CNTs has the relationship between n and f_0 due to the same reason as the single-wall CNTs, the characteristics of the BPF can be determined by means of the dimension of the bundle CNT. That is, this device may work as a discriminator of the number of CNTs and diameter of the each CNT in the bundle, respectively.

From Figs. 10 and 11, operating frequency f_0 reaches nearly 1 THz but the minimum insertion loss $IL_{\min}$ is about 9dB when m is 50. We may then realize an oscillator with operating frequency up to one THz if we could use a circuit made of an amplifier and a feedback loop whose total gain is more than 9dB.

IV. CONCLUSION

We have analyzed dispersion curves of magnetostatic waves in YIG excited by CNT electrodes based upon the magnetostatic approximation method. It is found that such magnetostatic waves have the wavelength as small as several nanometers and operate at the frequency in THz domain. We have verified our calculation by comparing with experimental data in Ni. We have studied the band-pass filter characteristics of the YIG device where the high-frequency current flowing on single-wall CNTs. The characteristics of IL-frequency, $IL_{\min}$, f_0 and BW have been evaluated varying the diameter or the chirality of the CNT. As a result, it is found that we can design the BPF by means of diameter of the CNT and improve the operation frequency into THz region.

To reduce the IL for practical application, we have proposed a BPF with bundle CNTs as electrodes. $IL_{\min}$ is found to be improved from 27.5dB to 9.0dB by using bundle CNTs with m=50 instead of single-wall CNTs.

On these results, we have proposed a novel ferrite device which will operate as a discriminator of the chirality of CNTs and the number of CNTs in a bundle CNT. In this device, the chirality and the number of CNTs in a bundle CNT may be measured by means of the band-pass characteristics via operating wavelength.

From the m-dependence of the $IL_{\min}$, f_0, and BW, we have proposed feasibility to realize an oscillator up to one THz, where we need a circuit consisting of an amplifier and a feedback loop whose total gain is more than 9dB.

ACKNOWLEDGEMENT

The author would like to acknowledge Drs. S. Uemura in Noritake Co., Limited and M. Kusunoki in Japan Fine Ceramics Center for their helpful discussion.

APPENDIX A: DERIVATION OF AMPLITUDE *D*

The right hand side of Eq.(10) can be expressed as the integrated form when N goes to infinity:

$$\lim_{N\to\infty}\sum_{i=0}^{2N} e^{|\beta|(-r+x_i)}\tilde{J}_i^z(\beta) = \frac{I_0}{\pi}\int_0^{\pi} e^{|\beta|r(-1+\cos x)}\cos(\beta r\sin x)dx \tag{A1}$$

Applying the Bessel's integration formalism to the R.H.S. of Eq. (A1), we obtain

$$\frac{I_0}{\pi}\int_0^{\pi} e^{|\beta|r(-1+\cos x)}\cos(\beta r\sin x)dx = I_0 e^{-|\beta|r}J_0(0) \tag{A2}$$

where $J_0(0)$ is the 0-th Bessel function. Noting $J_0(0) = 1$, Eq.(A2) can be expressed as

$$\text{w} \lim_{N\to\infty} \sum_{k=0}^{2N} e^{|\beta|(-r+x_k)} \tilde{J}_k^z(\beta) = I_0 e^{-|\beta|r}. \quad \text{(A3)}$$

Finally the amplitude D can be expressed as

$$D = -\frac{I_0 e^{-|\beta|r}}{4\pi j\beta F(\omega,\beta)p(\omega,\beta)}. \quad \text{(A4)}$$

APPENDIX B: DERIVATION OF THE ADDITIONAL FREQUENCY DUE TO THE SPIN INTERACTION

Consider a schematic model with an array of 1-dimensional electronic spins as shown in Figure 13. The motion of equation for the magnetization $\boldsymbol{M}$ of the spin can be described as follows similar to Eq. (16) in [11]:

$$\frac{d\boldsymbol{M}_i}{dt} = -\gamma\mu_0 \boldsymbol{M}_i \times \boldsymbol{H}_i, \quad \text{(B1)}$$

where i implies the site of the spin. The exchange magnetic field which acts on the i-th spin is

$$\boldsymbol{H}_i = \lambda(\boldsymbol{M}_{i-1} + \boldsymbol{M}_{i+1}), \quad \text{(B2)}$$

where λ corresponds to the Weiss's molecular field. In general, the magnetization $\boldsymbol{M}_i$ can be represented in the polar coordinate as

$$\boldsymbol{M}_i = M_s(\sin\theta_i\cos\psi_i, \sin\theta_i\sin\psi_i, \cos\theta_i). \quad \text{(B3)}$$

Assuming that the motion of electronic spins is in the equilibrium, θ_i is nearly equal 0 when the high-frequency magnetization is quite smaller than the bias magnetization, and the phase-difference between neighboring electrons $\Delta\psi$ is constant, we can obtain the followings, respectively:

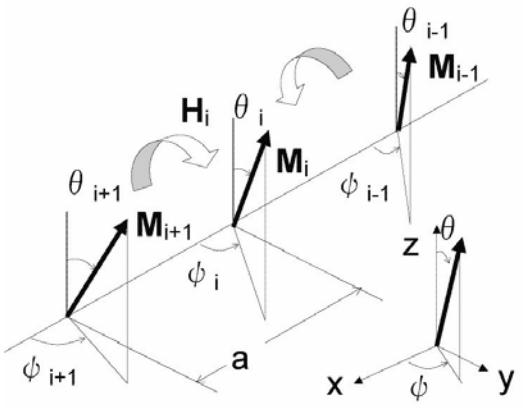

Fig. 13: Schematic model of the spin-exchange's addition to the resonance frequency of the ferrite in bias magnetic field with z-direction.

$$\frac{d\theta_i}{dt} = 0, \quad \text{(B4a)}$$

$$\theta_i = \theta_{i+1} = \theta_{i-1} \cong 0, \quad \text{(B4b)}$$

$$\Delta\psi \equiv \psi_{i+1} - \psi_i \cong \psi_i - \psi_{i-1} \equiv k_x a, \quad \text{(B4c)}$$

where k_x is the wave number of magnetostatic wave, a is the distance between neighboring electronic spins in Figure 13. These assumptions are similar to those adopted in the derivation of spin waves in the literature [11]. Substituting Eqs. (B2), (B3) and (B4) into Eq. (B1), we can obtain

$$\frac{d\psi_i}{dt} = 2\gamma\mu_0\lambda M_s(1-\cos k_x a). \quad \text{(B5)}$$

When $H_e \equiv \lambda M_s$ and $\omega_{he}(\beta) \equiv d\psi/dt$, Eq. (B5) becomes

$$\omega_{he}(\beta) = 2\gamma\mu_0 H_e(1-\cos k_x a), \quad \text{(B6)}$$

which is added to the magnetic resonance frequency ω_h of conventional permeability and the permeability becomes as shown in Eqns. (3) and (4).

REFERENCES

[1] P. C. Fletcher, C. Kittel, "Consideration on the Propagation and Generation of Magnetostatic Waves and Spin Waves," *Phys. Rev.*, vol. 120, pp. 2004-2006 (1960); M. Nakajima, "The microwave engineering," *Morikita publishing*, 1989 (in Japanese).

[2] S. N. Bajpai, R. L. Carter, and J. M. Owens, " Insertion Loss of Magnetostatic Surface Wave Delay Lines," IEEE Trans. vol. MTT-36, pp. 132-136, 1988.

[3] S. Iijima, "Helical Microtubules of Graphitic Carbon," Nature (London), vol. 354, pp.56-58, 1991.

[4] S. Lim, D. Ciuparu, C. Pak, F. Dobek, Y. Chen, D. Harding, L.D. Pfefferle, and G. Haller, "Synthesis and Characterization of Highly Ordered Co-MCM-41 for Production of Aligned Single Walled Carbon Nanotubes (SWNT)," J. Phys. Chem. B, vol. 107, no. 40, pp. 11048-11056, 2003.

[5] Xu-Hui Sun, Chi-Pui Li, Wing-Kwong Wong, Ning-Bew Wong, Chun-Sing Lee, Shuit-Tong Lee, and Boon-Keng Teo, "Formation of Silicon Carbide Nanotubes and Nanowires via Reaction of Silicon (from Disproportionation of Silicon Monoxide) with Carbon Nanotubes," J. Am. Chem. Soc., vol. 124, pp. 14464-14471, 2002.

[6] R. Bauminger, S. G. Cohen, A. Marinov, and S. Ofer, "Study of the Internal Fields Acting on Iron Nuclei in Iron Garnets, Using the

Recoli-Free Absorption in Fe57 of the 14.4-keV Gamma Radiation from Fe57," Phys. Rev., vol. 122, pp. 743-748, 1961.

[7] Y. Ishikawa, T. Nomoto, T. Okada, S. Shinmura, F. Kanaya, S. Ichiguchi and T. Umegaki, "A Signal-to-Noise Enhancer with Extended Bandwidth Using Two MSSW Filters and Two 90o Hybrids," IEICE Trans. Electron., vol. E78-C, no. 8, pp. 1026-1032, 1995.

[8] P. R. Emtage, "Interaction of magnetostatic waves with a current," J. Appl. Phys., vol. 49, pp. 4475-4484, 1978.

[9] R. Saito, G. Dresselhaus and M. S. Dresselhaus, "Trigonal warping effect of carbon nanotubes," Phys. Rev., vol. B61, pp. 2981-2990, 2000.

[10] T. Umegaki, M. Ogawa, Y. Makino, and T. Miyoshi, "Quantum Transport in Carbon Nanotubes with Arbitrary Chirality," Memoirs Graduate School Science & Technology, Kobe University, vol. 22-A, pp. 103-114, 2004.

[11] C. Kittel, "Introduction to Solid State Physics (seventh edition)," John Wiley and Sons, Inc., 1996.

[12] H. A. Mook and D. McK. Paul, "Neutron-Scattering Measurement of the Spin-Wave Spectra for Nickel," Phys. Rev. Let., vol. 54, no. 3, pp. 227-229, 1985.

T. Umegaki received the B.E. and M.E. degrees from Kyoto Institute of Technology, Japan, in 1991 and 1993, respectively. He joined Murata Manufacturing Co., Ltd., Kyoto, Japan, in 1993 and had engaged in development of radio-frequency devices until 2001. He is currently pursuing the Ph.D. degree in graduate school of science and technology, Kobe University, Japan.

M. Ogawa received the B.E., M.E., and Dr. of Eng. degrees in electronic engineering from the University of Tokyo, Tokyo, Japan, in 1980, 1982, and 1985, respectively. In that year, he became a research associate at the Department of Electronics, Kobe University. From 1992 to the end of 1993, he was on leave at IBM T.J. Watson Research Center in New York as a Visiting Scientist. He is now a full Professor at Kobe University. He has been engaged in research on nano-scale MOS devices, quantum devices, and photo-electronic devices. He is a member of the IEEE and the Japan Society of Applied Physics.

T. Miyoshi received the B.S. in electrical engineering from the University of Tokyo, Tokyo, Japan, in 1967, and the M.S. and Ph.D. degree in electronics engineering from the University of Tokyo, Tokyo, Japan in 1969 and 1972, respectively. In 1972 he was appointed Lecture, and from 1974 to 1987, he was an Associate Professor in the Department of Electronics Engineering, Kobe University, Kobe, Japan, where he is presently a Professor. He has been engaged in research of electromagnetic-wave theory, microwave integrated circuits, and light-wave electronics. His current research includes quantum transport modeling in nanostructures. In 1976 he was a Visiting Scholar at McGill University, Montreal, Que., Canada. From 1982 to 1984, he was a Visiting Scientist at Bell Laboratories, Holmdel, NJ. He is a member of the IEEE and the Japan Society of Applied Physics. He received a Yonezawa Award in 1974 and an Outstanding Book Award in 1977 both from the Institute of Electronics, Information and Communication Engineers in Japan.